Carbon 223 (2024) 119027

Contents lists available at ScienceDirect

Carbon

journal homepage: www.elsevier.com/locate/carbon

Research paper

# Development of long-range conductivity mechanisms in glass-like carbon

Jaspa Stritt *, Jerome A. Cuenca, Evan L.H. Thomas, Oliver A. Williams

*School of Physics and Astronomy, Cardiff University, Cardiff, UK*

ARTICLE INFO

*Keywords:*
Glass-like carbon
Dielectric spectroscopy
Microwave
conductivity

ABSTRACT

The conductivity mechanisms in glass-like carbon synthesised from SU-8 3005 photoresist are explored as a function of pyrolysis temperature (between 700–750 °C) utilising microwave dielectric spectroscopy techniques. Broadband measurements using an open-ended coaxial probe (BCP) are used to investigate the complex permittivity and conductivity as a function of frequency and show the development of long range conduction and $sp^2$ carbon chain formation. Fixed frequency resonance measurements using microwave cavity perturbation (MCP) methods are shown as a way of measuring this transition and change in Q-factor without requiring contacts and therefore acting as a effective method for non-destructive and non-invasive measurements. Using these methods we show a clear change in the AC conductivity of glass-like carbon at a pyrolysis temperature of ~730 °C and demonstrate how microwave cavity perturbation (MCP) can be used as a non-contact method of dielectric spectroscopy for determining the transition of conductivity mechanisms in glass-like carbon from short to long range and therefore as a method for non-destructive material quality control. We demonstrate that both BCP and MCP dielectric spectroscopy methods are effective at clearly detecting changes in the structure and conductivity mechanisms of glass-like carbon over a small pyrolysis temperature range.

## 1. Introduction

Glass-like carbon can be briefly described as a macro isotropic, non-planar form of non-graphitising carbon with resilience to high temperature in inert environments due to a high sublimation point (~3000 °C) and non-graphitising structure [1–3]. In recent years, glass-like carbon has been synthesised through the pyrolysis of organic resins in the form of photoresists for further use in a variety of micro-electrical-mechanical systems (MEMS) [4–6]. In addition, the electrical and refractory properties create exciting opportunities for the fabrication of miniature black body emitters [7].

The development of glass-like carbons structure through pyrolysis has been investigated in the past through a variety of methods including Raman spectroscopy, Transmission Electron Microscopy (TEM) and X-ray diffraction (XRD) [8,9]. However, whilst these studies have shown clear development in the structure over broad differences in pyrolysis/heat-treatment temperature, the development over small changes in pyrolysis temperature and the effects of these changes on the electrically conducting structure remains unclear. The structure of glass-like carbon is most commonly described through models describing the ribbon-like structure [2,10] and fullerene-related structure [11] which both describe the development of glass-like carbon through pyrolysis from an organic polymer in a process that maintains the morphology of the precursor without passing through a plastic phase.

Typically, these resins are pyrolysed in inert atmospheres to temperatures exceeding 900 °C. A common precursor in modern applications has been SU-8 photoresist, a negative epoxy-based photoresist originally developed by IBM [12]. The major steps of pyrolysis include **Pre-carbonisation** (elimination of solvent and unreacted monomer at temperatures below 300 °C), **Carbonisation** (the elimination of oxygen, hydrogen and halogens as well as the development of an interconnected polymer-like $sp^2$ carbon structure at temperatures of 300 °C <T <1200 °C) and **Annealing** (eliminating defects/impurities and further increases the inter-connectivity of the carbon network) [5]. Previous studies have shown conductivity to increase rapidly with pyrolysis at temperatures within the carbonisation step [13,14].

In this work, Raman spectroscopy and UV–visible spectroscopy are both used as initial indication of $sp^2$ carbon developing from SU-8 3005 as a result of pyrolysis to glass-like carbon. The development of an interconnected $sp^2$ carbon network during the carbonisation step of pyrolysis and its impact on the development of long-range conductivity is then investigated through the use of microwave dielectric spectroscopy techniques at both broadband frequency ranges and fixed frequencies using broadband coaxial probe (BCP) and microwave cavity perturbation (MCP) methods, respectively, as ways to more accurately determine temperature ranges in which these material and electrical

* Corresponding author.
*E-mail address:* strittj@cardiff.ac.uk (J. Stritt).

https://doi.org/10.1016/j.carbon.2024.119027
Received 12 December 2023; Received in revised form 6 March 2024; Accepted 7 March 2024
Available online 11 March 2024

transitions occur. The methods presented are shown to be an effective means of quality control in the production of high quality glass-like carbon in practical production settings, ensuring that dominant long-range conductivity mechanisms are present whilst optimising the pyrolysis temperature for efficient material synthesis. In addition, MCP is shown to be an effective method of quickly determining these qualities without contact or damage to the samples and without excessive processing. MCP also offers valuable insight in the dielectric properties of glass-like carbon, and its potential applications as an absorber at microwave frequencies.

## 2. Theory

### 2.1. Complex permittivity

The complex representation of relative permittivity ($\epsilon_r(\omega) = \epsilon'_r(\omega) - j\epsilon''_r(\omega)$) is able to describe a dielectric materials response in an alternating electric field where $\epsilon'_r(\omega)$ is the dielectric constant, $\epsilon''_r(\omega)$ is the dielectric loss factor, $j$ is the imaginary number $\sqrt{-1}$ and $\omega$ is the angular frequency. The conductivity for a percolating sample can then be approximated using the samples dielectric loss factor [15]:

$$\epsilon''_r(\omega) \approx \frac{\sigma}{\omega_{AC}\epsilon_0} \tag{1}$$

where $\epsilon_0$ is the permittivity of free space, and $\sigma$ is the frequency dependent AC conductivity.

### 2.2. Percolation & AC conductivity universality

In order to achieve long-range conductivity between two nodes, an uninterrupted path (or multiple paths) of conducting pathways must exist between those nodes. The fulfilment of this condition can be described through percolation theory [16,17]. We can consider an infinite network of nodes which can either be connected to a neighbour by a conducting pathway or not. An insulator would be modelled by a series of non-connected nodes, whilst a metallic material would be represented by a fully connected network. For an arbitrary material containing nodes which are randomly connected to neighbours according to a probability ($p$), the material will exhibit conducting chains of various different sizes. Logically, if this probability ($p$) is low, then the average length of chains will also be lower, and as $p$ increases to 1, the network will become increasingly more connected. If $p$ is greater than a value $p_c$ (the percolation threshold), then the material will exhibit interconnected chains that are of a size in the order of the network size. The result in a macroscopic material is DC conductivity between any two arbitrary points. Fig. 1 shows how varying $p$ affects the connectivity of the network and percolation. At this percolation threshold, the material will becomes conducting to direct current, and as $p$ continues to increase, the DC conductivity of this network will also increase.

If we consider a material with a network that is connected below the percolation threshold (e.g. Fig. 1a) being subject to an alternating electric field, then at low frequencies the AC conductivity will be close to 0 as the path length of electrons in the material will be significantly longer than the mean path length in the network. As the frequency of the electric field ($\omega$) is increased, the path length of electrons will decrease and the longest chains (those longer than the length travelled by electrons) will exhibit AC conductivity. As $\omega$ continues to be increased, these electrons are able to oscillate freely within shorter chains and therefore the AC conductivity increases.

For a material with a conducting network connected at or above the percolation threshold (eg. Figs. 1c & 1d), assuming that the sample is macroscopic, the main structure within the network will give rise to long-range conductivity across the sample. The AC conductivity will present as a static value extending to $\omega = 0$ (long-range conductivity) which then starts to rise at a given frequency known as the onset frequency ($\omega_{onset}$). The relationship between long-range conductivity ($\sigma_0$) and onset frequency is defined by a Jonscher type power law formalised as the Almond–West (AW) formula [19–21]:

$$\sigma(\omega) = \sigma_0 + \sigma_0 \left(\frac{\omega}{\omega_{onset}}\right)^n \tag{2}$$

where $\sigma(\omega)$ is the frequency dependent AC conductivity and $n$ is a value determined by the conductivity mechanisms involved [22]. By normalising the AC conductivity to the measured long range conductivity ($\sigma_0$), it is made easier to observe the development of onset frequency as the AC conductivity begins to rise due to shorter chains beginning to contribute to overall AC conductivity at higher frequencies, thus allowing us to see a response that shows the effect of increasing percolation within a network and revealing the AC conduction mechanisms as shown previously [19,23,24].

$$\frac{\sigma(\omega)}{\sigma_0} = 1 + \left(\frac{\omega}{\omega_{onset}}\right)^n \tag{3}$$

When the frequency ($\sigma$) is equal to the onset frequency ($\sigma_0$), Eq. (3) simplifies to $\sigma_{onset} = 2\sigma_0$, allowing us to extract the onset frequency from the normalised data.

In Fig. 2, the normalised AW formula (Eq. (3)) is plotted for a series of arbitrary onset frequencies. At high frequencies (above the onset frequency), the second term of the AW formula dominates, resulting in a power-law relationship between frequency and conductivity ($\sigma(\omega) \propto \omega^n$).

The relationship between onset frequency and percolation can be explained by considering the conductivity behaviour of differently sized conducting chains, and the average conducting chain length within a material. In order for a conducting chain to respond efficiently to an applied alternating electric field, electrons within the chain must be able to oscillate freely along the length of the chain. This means that at low frequencies, electrons in short chains are not able to oscillate efficiently due to the electron path length being longer than the length of the chain. However, as the AC frequency is increased, electrons are able to oscillate efficiently in increasingly shorter chains, thus increasing the overall contribution to AC conductivity in the material. In materials with low connectivity (due to a low value of $p$ – as seen in Figs. 1a & 1b), the number of isolated chains is high and the average conducting chain length is low. In this case, at lower frequencies, very few conducting chains are able to efficiently host an alternating current, but this number rises as the AC frequency increases – thus leading to the observed power law.

However, as $p$ increases and the network becomes more highly interconnected (as seen in Figs. 1c & 1d), shorter chains are eliminated as they are incorporated into the percolating pathway or longer isolated chains. This results in the AC conductivity at lower frequencies increasing due to the number of longer chains increasing, but it also results in the number of short chains decreasing and therefore higher frequencies are needed in order to oscillate electrons quickly enough for the shortest chains in the network to contribute to the overall AC conductivity, thus resulting in the phenomenon of onset frequency increasing with percolation.

## 3. Experimental methods

### 3.1. Sample preparation

SU-8 3005 photoresist was spun onto 12 mm round fused-silica substrates at a speed of 2000 rpm for 45 s proceeded by a soft bake at 110 °C. The samples were then flood exposed to broadband UV light from a mercury-xenon gas lamp in order to form cross links between the epoxy groups to form a large polymer network followed by post-exposure bake also at 110 °C. The samples were then placed into an Inconel Alloy 600 tube furnace. The tube then underwent 3 purge cycles of being evacuated to 2mbar and flooded with Argon up

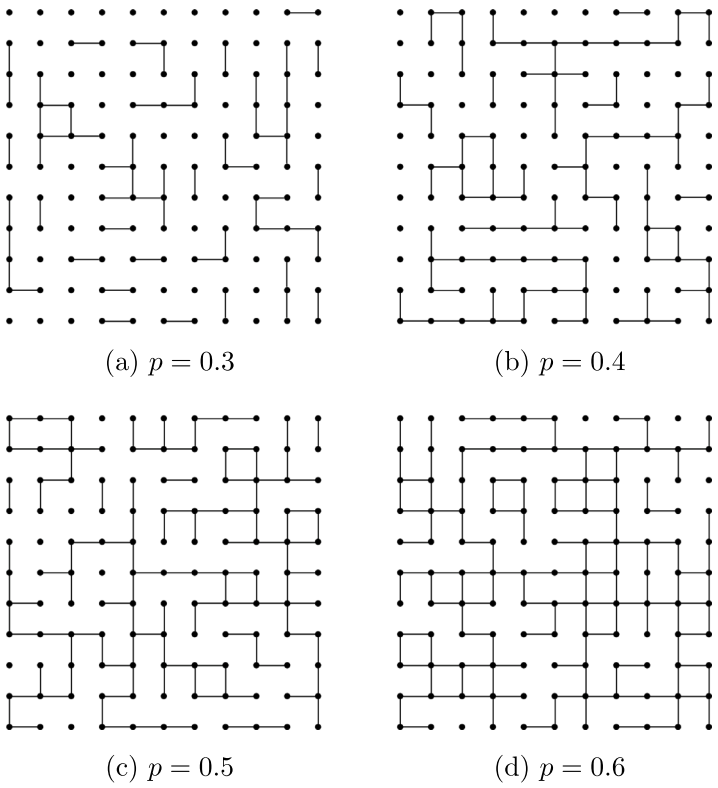


**Fig. 1.** Varying probability for each pair of neighbouring nodes in a 2D square lattice to be connected. For a 2D lattice, the percolation threshold ($p_c$) is 0.5 and percolation is evident at $p = 0.5$ and $p = 0.6$. At $p = 0.3$ an abundance of short and isolated chains exist with longer chains beginning to form at $p = 0.4$, but percolation across the lattice does not yet exist. [18].

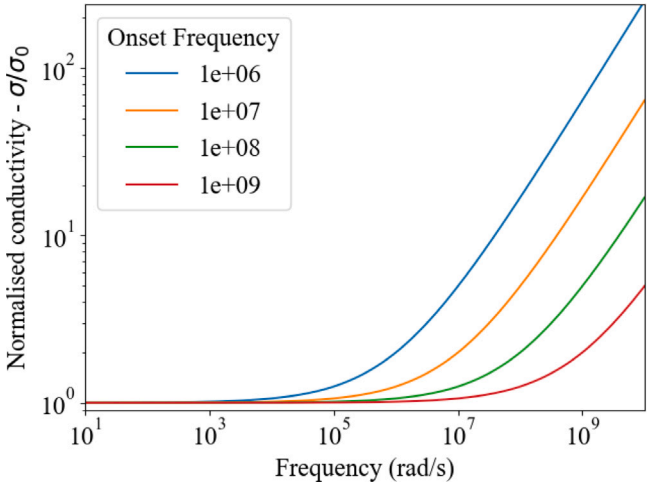


**Fig. 2.** Almond–West model normalised to DC conductivity for a set of arbitrary onset frequencies.

to 500 mbar. After purging, the furnace was once again evacuated to 2 mbar before introducing a constant flow of 200SCCM of Argon and maintaining a pressure of 50mbar. The samples were initially heated from room temperature to 300 °C at a rate of 2 °C/min and held at this temperature for 1 h. The samples were then heated to their maximum pyrolysis temperature (ranging from 500–900 °C) at a rate of 5 °C/min and again held at this maximum temperature for 1 h. The samples were then allowed to cool back to room temperature before being removed from the tube furnace.

### 3.2. Raman spectroscopy

Raman spectra were collected using a *Horiba LabRAM HR Evolution Raman spectrometer* at an excitation wavelength of 532 nm. For each sample, an average was calculated for 3 data sets for each sample, each consisting of 3 accumulation periods of 10 s. The laser power was adjusted to result in the maximum output signal for each sample whilst ensuring the sample remained undamaged by the laser.

### 3.3. Ultraviolet–visible spectroscopy

Ultraviolet–visible spectra were collected using a *Filmetrics F20 thin-film analyzer* in a transmission setup between 380–1050 nm, using a Si (silicon) wafer as an absorption standard for calibration.

### 3.4. Van der Pauw DC conductivity

Samples underwent further photo-lithographic processes to create a 'clover-leaf' pattern suitable for Van der Pauw DC conductivity measurements [25]. nLOF 2020 photoresist was spun onto the samples, patterned using a *Microwriter ML3* direct-write photolithography tool and developed in order to use as an etch mask for ICP-RIE etching utilising a *Oxford PlasmaPro 100 Cobra* ICP-RIE etch tool. Silver conductive paste was then applied to each of the arms of the clover-leaf and 4-point I-V measurements following the Van der Pauw technique were collected for each of the samples using a *Keysight B2902B Precision Source/Measure Unit* at room temperature.

### 3.5. Broadband coaxial probe

The Broadband Coaxial Probe (BCP) method, utilised a coaxial probe that terminates in free space. A dielectric sample was carefully compressed onto the aperture of opened ended probe, allowing the

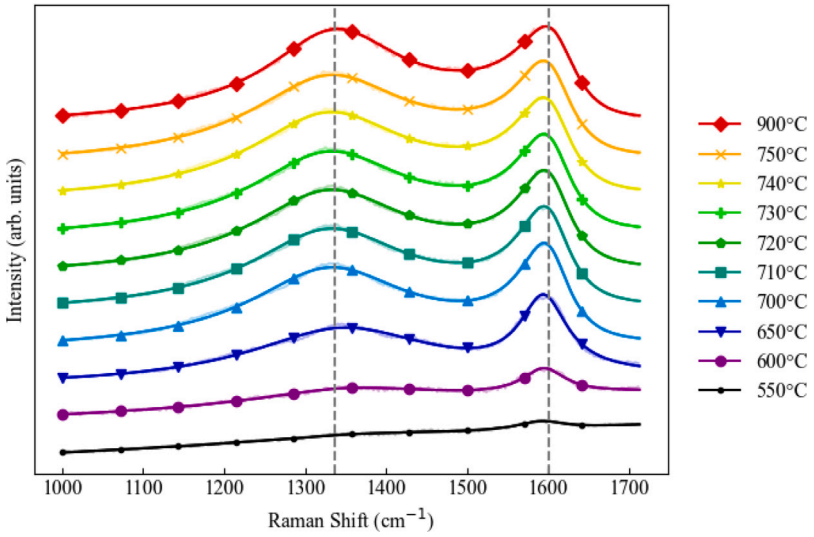


**Fig. 3.** Raman spectroscopy at 532 nm of SU-8 3005 pyrolysed at temperatures between 500–900 °C with fitted curves at the D & G bands.

electric field that extends from the open end of the coaxial probe to penetrate into the dielectric material. By analysing the change in reflection coefficient between the free space and dielectric terminated coaxial probes, it is possible to calculate the complex permittivity of the dielectric material [26]. Measurements of reflection coefficient were conducted using a coaxial probe connected to an *Keysight E4990A* impedance analyser (IA) & a *Keysight E5071C* vector network analyser (VNA) in an $S_{11}$ arrangement (reflected signal). The choice of analyser allowed for the selection of differing broadband frequency ranges that could be measured over, with the IA able to measure lower frequencies (~100 Hz–10 MHz) and the VNA able to measure frequencies in a higher range (~1 MHz–10 GHz).

### 3.6. Microwave cavity perturbation

In the Microwave Cavity Perturbation (MCP) method, a dielectric sample was placed inside an alternating electric field of a microwave cavity resonator in such a way as to perturb the field and alter the systems resonant frequency. The shift in resonance frequency ($\Delta\omega$) is attributed to a change in dielectric constant ($\epsilon_r'(\omega)$), whilst the dampening of the resonance in the cavity (as defined by the Q-factor) is attributed to the dielectric loss factor ($\epsilon_r''(\omega)$) [27]. The alternating electric field was applied using a *Keysight E5071C* vector network analyser (VNA) to a split cylindrical dielectric resonator operating with the TE011 mode with the resulting resonance being measured by the VNA in an $S_{21}$ transmission arrangement [28]. This method requires no physical contacts to be made with the sample.

## 4. Results & discussion

### 4.1. Raman & optical absorption spectroscopy

The structural development of glass-like carbon arises through the elimination of non-carbon atoms from the polymeric structure of the cross-linked SU-8 molecules. Fig. 3 shows Raman spectroscopy data collected at an excitation wavelength of 532 nm. The disordered D-band found at ~135 0 cm$^{-1}$ attributed to the breathing mode of graphitic rings and the graphitic G-band found at ~1580–1620 cm$^{-1}$ attributed to the in-plane bond stretching modes between pairs of sp$^2$ hybridised carbon atoms are both evidence for the presence of sp$^2$ carbon [29,30] and can be clearly seen to develop with pyrolysis temperature. Glass-like carbon consists of an entirely sp$^2$ structure, and so we would expect to see the G band develop at ~1600 cm$^{-1}$ [29].

Whilst the development of the D & G bands is clear, it is difficult to correlate structural change and changes in conductivity with pyrolysis temperature. This is particularly true in the region of 700–900 °C where there is little to no change in the D & G peaks.

Optical absorption spectroscopy scans (Fig. 4) show an increasing pyrolysis temperature leading to a sharp increase in optical absorption. SU-8 samples pyrolysed to 550 °C exhibit optical transmission increasing across the measured range (380–1050 nm) resulting in high transmission (above 60%) above 650 nm. The optical absorption then increases steadily with temperatures below 700 °C across the measured range and then sharply at temperatures about 700 °C to absorption levels above 90% across the entire optical range. Fig. 5 shows images of both non-pyrolysed SU-8 and 2 samples significantly above and below the transition temperature (~700 °C) with the increase of absorption in the optical range being evident.

Whilst the fused-silica substrates exhibit a band gap far exceeding the highest energy in the measured range [31,32] resulting in high transmission, and the SU-8 photoresist is reported to having high transmission in the optical range above 400 nm [33], glass-like carbon exhibits a band-gap that develops with pyrolysis/heat-treatment to values below 1 eV [34,35], resulting in the observed increased in opacity. Above 700 °C however, changes in absorption between samples at varying pyrolysis temperatures begin to reduce significantly to the point where noise dominates. Similar to Raman spectroscopy, the changes in optical absorption signal at pyrolysis temperatures beyond 700 °C are very small, making it difficult to use optical absorption as a method to correlate pyrolysis temperature to structural change at temperatures within the carbonisation process of pyrolysis.

### 4.2. Van der Pauw DC conductivity

The DC conductivity of pyrolysed SU-8 films was measured and analysed using the Van der Pauw technique utilising a clover-leaf geometry. The resultant conductivity as a function of pyrolysis temperature is presented in Fig. 6(a). The DC conductivity clearly increases by almost 2 orders of magnitude between 700–750 °C (from ~2 S/m to ~150 S/m). This increase is due to percolating pathways within the material developing and whilst low pyrolysis temperatures exhibit a low DC conductivity, the existence of a measurable conductivity indicates the existence of a percolating pathway and thus a network that is connected above the percolation threshold. The increase in conductivity above the percolation threshold for a disordered material is exponential [36] and is observed in the Van der Pauw measurements for SU-8 as a function of pyrolysis temperature.

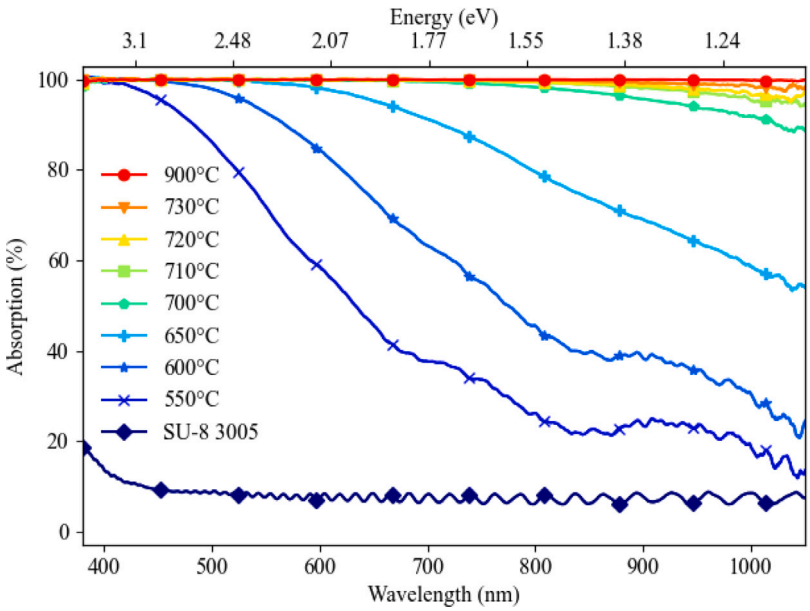


**Fig. 4.** Transmission mode ultraviolet–visible spectroscopy of non-pyrolysed SU-8 3005 and SU-8 3005 pyrolysed at varying temperatures between 500–900 °C.

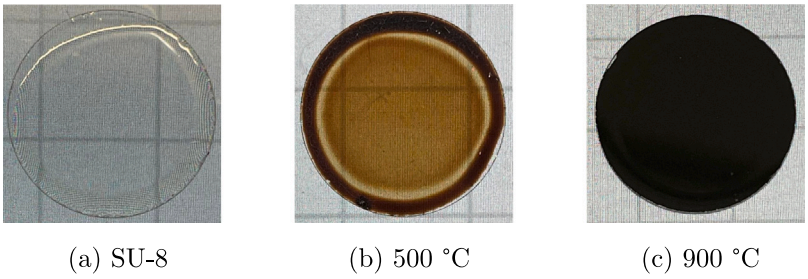


**Fig. 5.** Images of three (12 mm diameter) samples at varying states of pyrolysis, (a) unpyrolysed SU-8 3005, (b) & (c) pyrolysed up to 500 °C and 900 °C respectively.

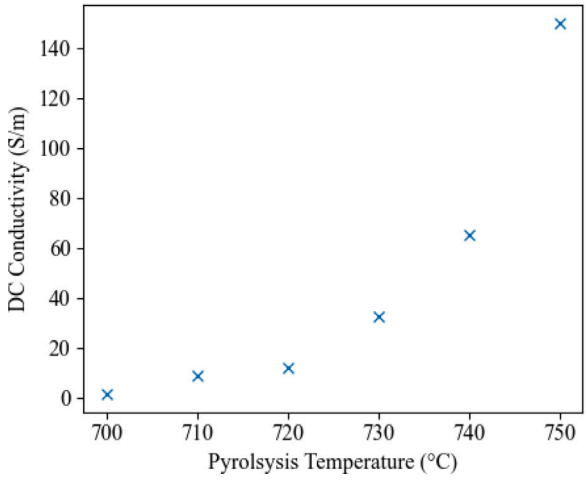


**Fig. 6.** DC Conductivity for SU-8 3005 photoresist pyrolysed between 700–750 °C. (a) As measured using Van der Pauw technique utilising a clover-leaf geometry). (b) Comparison between normalised DC conductivity acquired from Van der Pauw technique and Broadband Coaxial Probe.

Whilst the traditional Van der Pauw technique for measuring DC conductivity does show a development in conductivity, this method requires extensive sample preparation. By using a clover-leaf geometry, errors caused by non-ideal contacts are eliminated [25]. However, this creates additional work by requiring a series of photo-lithographic processes to be completed to achieve this geometry. More commonly, square or circular geometries are used to minimise the amount of sample preparation required. But the existence of an edge bead, from spinning the SU-8 onto the sample (which persists in the sample through pyrolysis), means that some form of edge bead removal would be required — thus still introducing further processing steps.

### 4.3. Broadband coaxial probe

Using Eq. (1), we can calculate the frequency dependent AC conductivity from the measured dielectric loss factor. Fig. 7 shows the measured effective AC conductivity (long-range conductivity scaled to values for DC conductivity as measured using Van der Pauw technique) between 1000 Hz and 1 GHz for samples pyrolysed between 700–750 °C. For all samples, conductivity is measured at a constant value for each pyrolysis temperature at lower frequencies (long-range conductivity), with conductivity then beginning to steadily increase (transitioning to short-range conductivity) above a certain frequency (the onset frequency). There is a clear increase in the long-range conductivity at lower frequencies (below ~1 MHz), increasing by almost 2 orders of magnitude between pyrolysis at 700 °C and 750 °C. Through structural (Raman) and optical spectroscopy methods, almost no change in this region is apparent, however the development of the long-range conductivity indicates the development of long range transport.

The fixed value for long-range conductivity, according to the AW formula, should extend to $\sigma = 0$, thus suggesting that this is equal

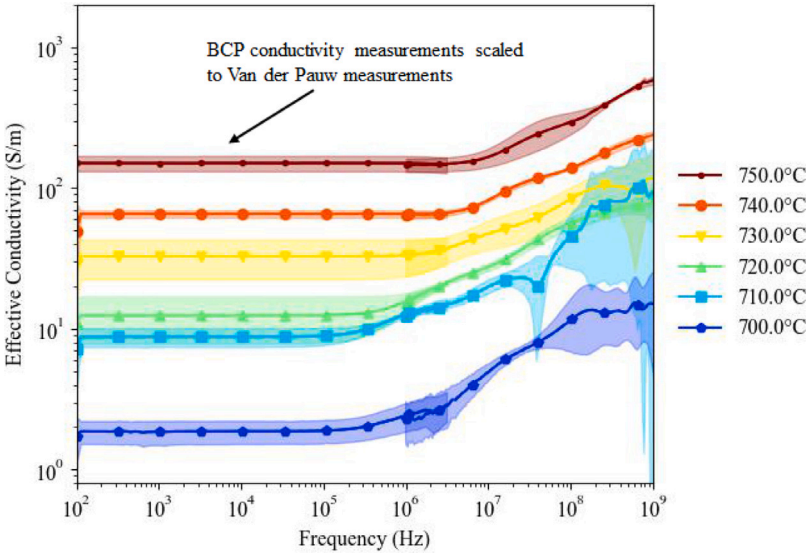


**Fig. 7.** Conductivity of SU-8 3005 pyrolysed at varying temperatures between 700–750 °C (Eq. (1)) with conductivity measured using BCP scaled to values for DC conductivity as measured using the Van der Pauw technique (Fig. 6).

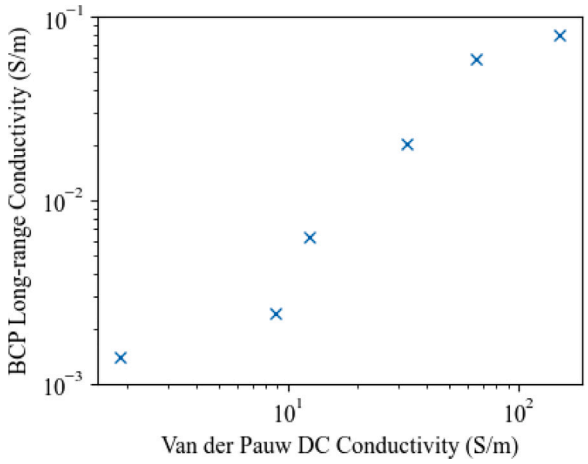


**Fig. 8.** Proportionality between long range conductivity measured using Van der Pauw and Broadband Coaxial Probe methods.

to the DC conductivity. However, in this case, a clear disparity between the values measured through Van der Pauw measurements and through BCP was observed. BCP requires the use of a model that assumes an infinite effective sample thickness in order to ensure that the electromagnetic field extending from the terminated coaxial probe is contained within the material being measured. Finite Element Modelling (FEM) of the BCP probe (provided in Fig. 9) was achieved using COMSOL Multiphysics (V5.3a) using the Electromagnetics module to obtain electric field plots and corroborate the capacitance model with the measured standards. Axisymmetric models were carried out using the frequency domain solver at 1 GHz.

FEM models show that the electric field, when a 1 mm thick quartz sample is present, reduces the E-field at the probe end when compared to an effectively infinitely thick quartz sample. Therefore Fig. 7 provides a more accurate depiction of the AC conductivity values by scaling the long range conductivity to the values for DC conductivity acquired using the Van der Pauw technique.

It should be noted however, that regardless of the specific values, the trends shown between samples within this method are still valid. Eq. (2) shows us that for frequencies below the onset frequency, the conductivity approximates to a fixed value that extends to $\omega = 0$ (DC conductivity). Once the AC frequency is greater than the onset frequency, we see an increase in AC conductivity as a function of frequency according to the AW formula (Eq. (2)). In Fig. 10, the AC conductivity is normalised across the measured range to the DC conductivity according to Eq. (3), due to a proportionality existing between these the long-range conductivity measured using these methods (shown in Fig. 8). This analysis method does not rely on specific values for conductivity, but instead is reliant on the conductivity mechanisms measured as the frequency is increased, and therefore does not rely on the infinite model theory to acquire values for onset frequency. There is a clear increase in onset frequency with an increase in pyrolysis temperature, with a significant increase occurring in samples pyrolysed at 730 °C and above. The onset frequency, extracted from Fig. 10 is shown in Fig. 11. This again shows the onset frequency increasing drastically between 720 °C and 730 °C.

During exposure of SU-8 to a UV broadband or i-line (365 nm) radiation source, cross links form between the epoxy groups of the SU-8 molecules. This process forms long polymer chains containing carbon, oxygen and hydrogen. Through the pyrolysis process, non-carbon atoms are eliminated, allowing for carbon atoms to form $sp^2$ hybridised bonds with each other whilst maintaining the morphology of the polymer before pyrolysis. By considering the carbon atoms as nodes within a conducting, this process of a developing $sp^2$ structure matches the development of AC conductivity as described by Dyre et al. This is seen clearly within the normalised conductivity data and matches the model described by the normalised AW-formula (Eq. (3)) as modelled in Fig. 2. The increased connectivity of the network and its effect on a frequency dependent AC-conductivity ($\sigma(\omega)$) and onset frequency ($\omega_{onset}$) can be described by theory surrounding percolation theory as discussed earlier and an increasingly interconnected network due to the probability of connected nodes ($p$) increasing.

BCP measurements are able to capture the development of the structure over a broadband frequency range and indicate development of long range electrical transport mechanisms. However due to the requirement that the material is in contact with the coaxial probe, delicate samples can be damaged in the measurement process.

### 4.4. Microwave cavity perturbation

Initial measurements of SU-8 3005 samples pyrolysed across wider temperature range (550–900 °C) were conducted to investigate any broad trends of pyrolysis on the ability for SU-8 3005 to act as an

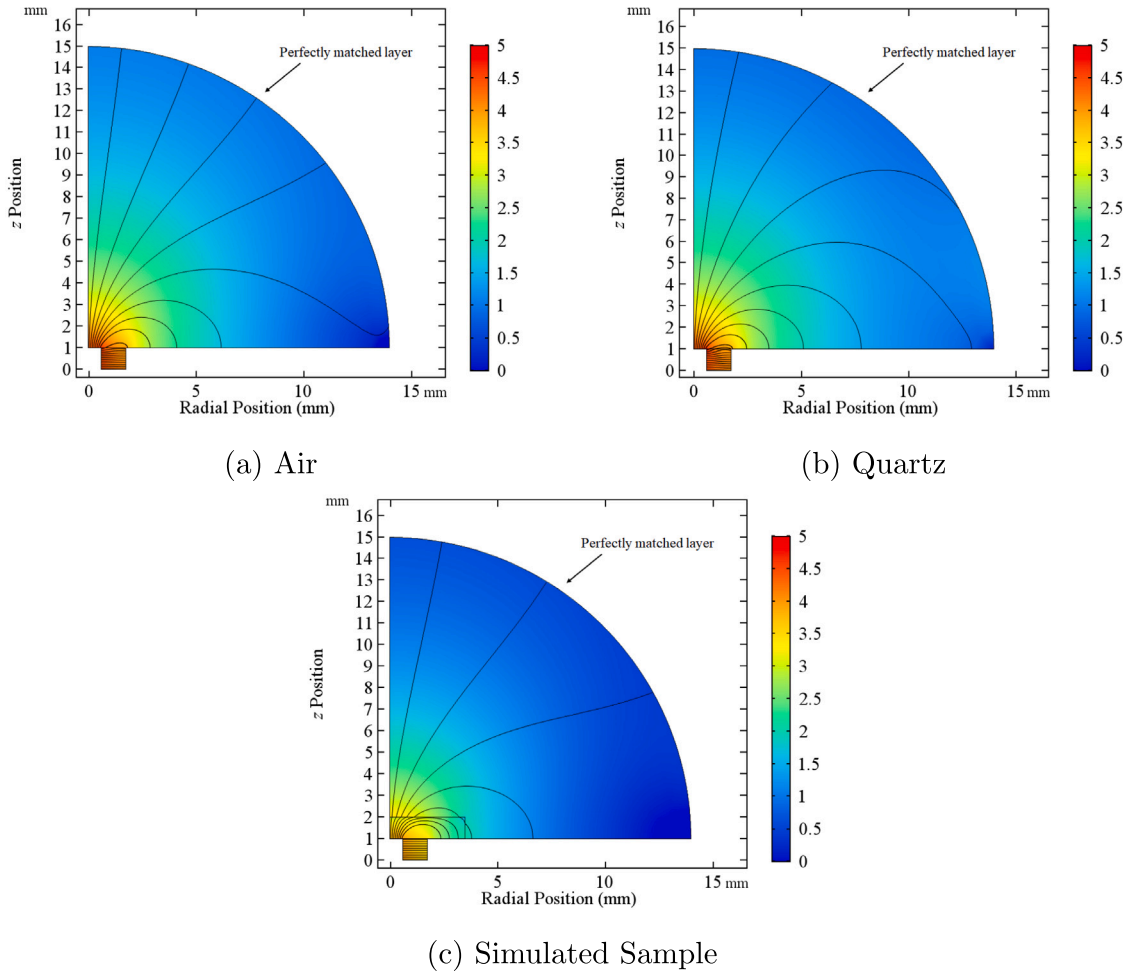


**Fig. 9.** FEM models for logarithmic electric field extending from coaxial probe into (a) air, (b) quartz (with effective infinite thickness) and (c) a finite thickness conducting film attached to a quartz substrate (simulating a sample).

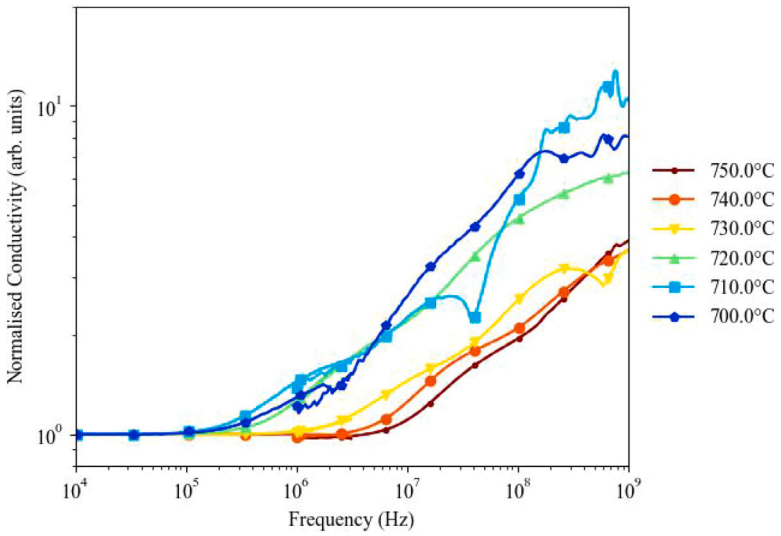


**Fig. 10.** Conductivity of SU-8 3005 pyrolysed at varying temperatures between 700–750 °C, normalised to DC conductivity.

effective microwave absorber. Q-factor values for the perturbed resonance peak at ~8.3 GHz are presented in Fig. 12. Q-factor (which is directly related to the dielectric loss factor, and therefore conductivity) can be seen to sharply decrease between pyrolysis at 700 °C and 750 °C, indicating structural change occurring due to pyrolysis in this region leading to a large increase in conductivity at ~8.3 GHz. This measurement was the leading motivation to investigate samples pyrolysed in the region of 700–750 °C.

The resonance response of a microwave cavity and the shifts of this response due to perturbation by both pyrolysed samples (in the

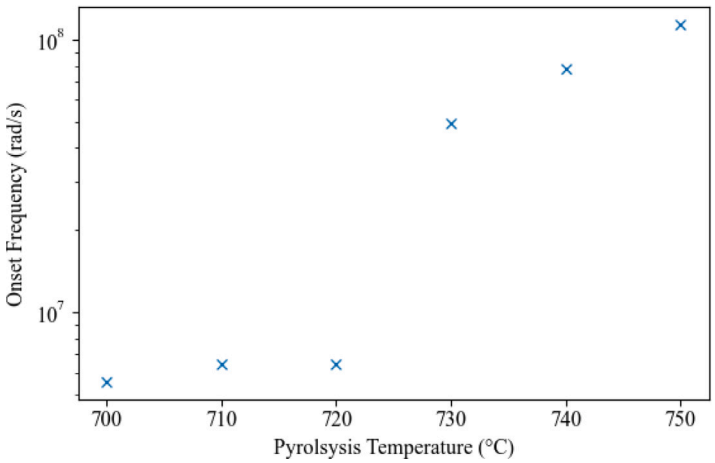


**Fig. 11.** Onset frequency as a function of pyrolysis temperature, extracted from conductivity data according to the AW Formula (Eq. (2)).

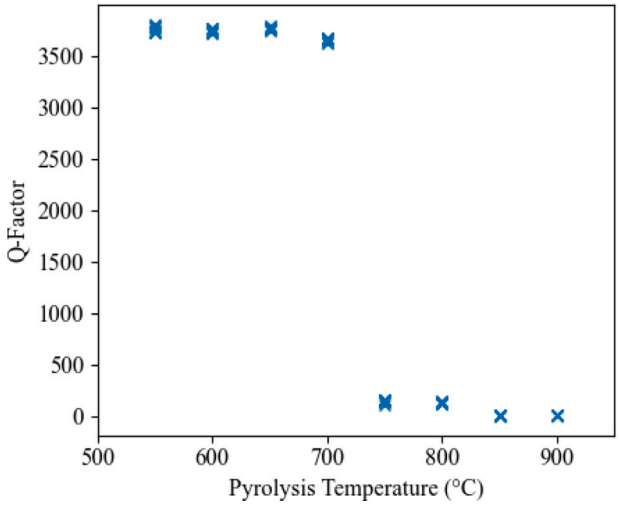


**Fig. 12.** Measured Q-factor for perturbed resonance peak due by SU-8 3005 samples pyrolysed between 550–900 °C (measured using microwave cavity perturbation with a resonance peak at ~8.3 GHz)

selected region of 700–750 °C) and reference samples (PTFE, quartz and non-pyrolysed SU-8) are presented in Fig. 13. The unperturbed peak can be found at ~8.3 GHz. Reference samples exhibit a clear shift in resonant frequency with PTFE shifting to ~8.29 GHz and quartz and non-pyrolysed SU-8 (on quartz) shifting the resonance to ~8.26 GHz. Pyrolysing the samples results in a clear dampening in the Q-factor of the cavity resonance with the FWHM of the peaks increasing by a factor of 13.5, whilst the peak centre of pyrolysed samples only decreases marginally. These shifts in the resonance response are directly linked and used to calculate both the dielectric loss factor (Fig. 14b) and relative dielectric constant (Fig. 14a) respectively.

The relative dielectric constant (seen in Fig. 14a), related to a materials ability to store energy through the efficient polarisation of a material due to an electric field (14a), can be seen to increase rapidly at 700 °C from ~5.5 to ~8.5 at 750 °C. Complex Permittivity measurements made by others at comparable frequencies for other carbon allotropes (including graphite, graphene and carbon nanotubes) show values for the relative dielectric constant increasing as a function of sample density and crystallite size, both of which are analogous to the loss of non-carbon material and increased connectivity of the carbon network in glass-like carbon as a result of pyrolysis [37,38].

The dielectric loss factor, related to losses in the material due to conductivity mechanisms being present can also be seen to increase dramatically in both the trace data (Fig. 13, through the clear broadening of resonance peaks with increase of pyrolysis temperature) and in the processed dielectric loss factor data (Fig. 14b). The dielectric loss factor starts to increase readily at 730 °C and continues to rise, exhibiting a response very similar to what we show through Van der Pauw DC measurements (Fig. 6) and BCP long-range conductivity . This indicates a sharp increase in the formation of conductivity mechanisms at the resonant frequency of the MCP method (~8.3 GHz). From BCP measurements, we can see that 8.3 GHz is well beyond the long-range response of glass-like carbon, and therefore any increases in dielectric loss will be due to the consolidation of short chains (that would otherwise not respond to the resonance peak) into larger chains and the main conducting network.

The trends measured using Van der Pauw, BCP and MCP methods are compared in Fig. 15. The trend between all three methods clearly show an agreement in the development of long-range conductivity, and display the exponential increase in conductivity that is expected for a disordered material above the percolation threshold [36]. However, MCP measurements offer the benefit of being completely non-contact and therefore can be used without risk of damage to the sample. This provides and excellent method for quality control and quantifying the change in Q-factor (and therefore dielectric loss).

## 5. Conclusions

Broadband Coaxial Probe (BCP) and Microwave Cavity Perturbation (MCP) methods of dielectric spectroscopy were used to investigate the development of long range conductivity mechanisms in glass-like carbon as a result of pyrolysis. Initial data from both Raman Spectroscopy and ultraviolet–visible spectroscopy were used to demonstrate structural changes in SU-8 3005 photoresist due to pyrolysis over a wide temperature, however both methods fail to effectively demonstrate structural change within the carbonisation step of pyrolysis that would lead to the development of long-range conductivity mechanisms. Van der Pauw DC conductivity measurements were also presented to show the development of DC (long-range) conductivity with pyrolysis, but requires considerable sample processing and does not provide insight into the short-range conductivity.

We have demonstrated how both BCP and MCP are effective in determining the development of long range conductivity mechanisms in glass-like carbon. Analysis of BCP data for glass-like carbon samples pyrolysed from SU-8 3005 in the region of 700–750 °C using percolation theory and the Almond–West (AW) model demonstrates both an increase in conductivity across the measured frequency range of almost 2 orders of magnitude whilst the shift in onset frequency demonstrates a significant development in the number of longer percolating pathways between samples pyrolysed at 720 °C and 730 °C. MCP methods

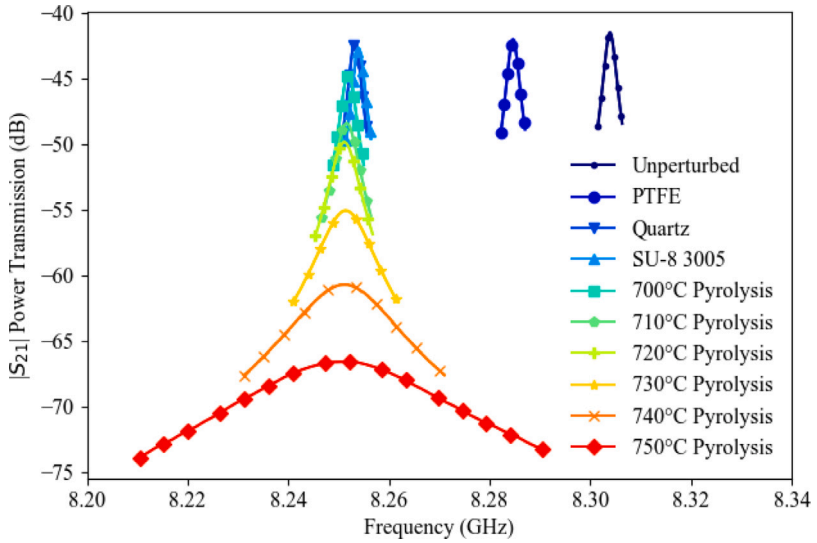


**Fig. 13.** Traces of resonance data for SU-8 3005 photoresist pyrolysed between 700–750 °C (measured using microwave cavity perturbation with a resonance peak at ~8.3 GHz).

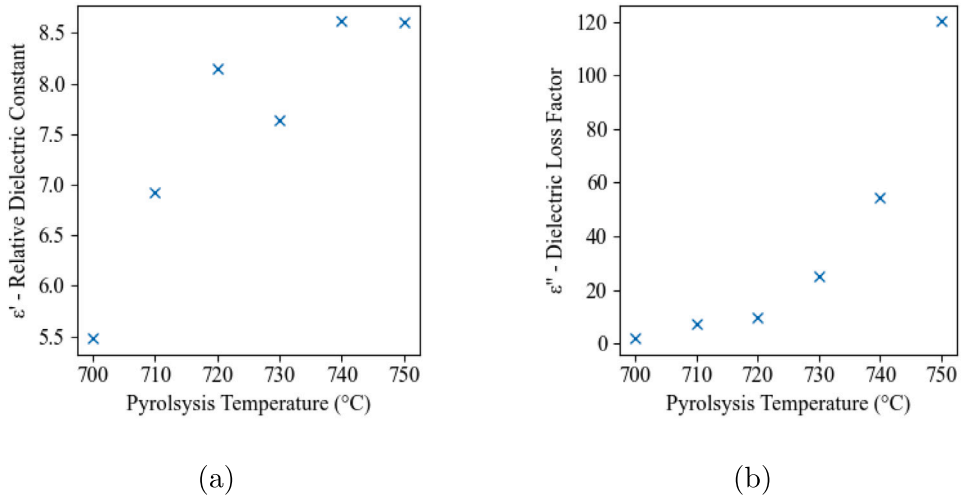


**Fig. 14.** Analysis of relative complex dielectric properties (as measured using microwave cavity perturbation method at ~8.3 GHz) to demonstrate the increase in both the (a) relative dielectric constant and (b) dielectric loss factor.

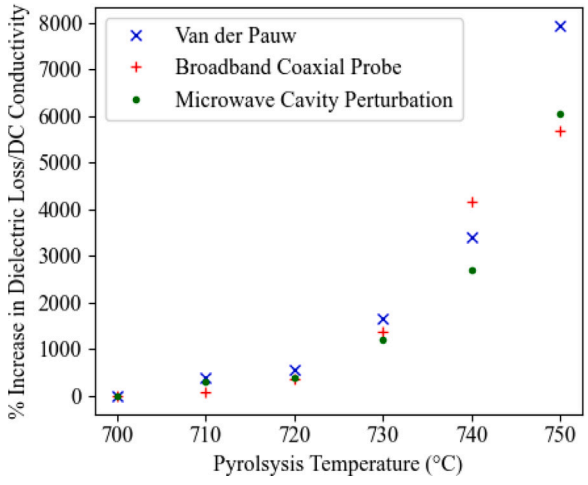


**Fig. 15.** The DC conductivity measured via Van der Pauw and BCP, and dielectric loss measured via MCP (related to the conductivity) for SU-8 samples pyrolysed between 700–750 °C are normalised and compared as a percentage increase from their values measured at 700 °C).

show a similar transition between these pyrolysis temperatures with the dielectric loss factor increasing rapidly at 730 °C, indicating an increase in both the average length and number of conducting pathways in the samples due to pyrolysis. Both of these dielectric spectroscopy techniques provide means of measuring this development at a significantly improved sensitivity compared to other techniques such as Raman and optical absorption spectroscopy, and significantly quicker & easier than Van der Pauw. MCP also provides a method for detecting the development of glass-like carbons $sp^2$ network through a non-contact method, allowing for the measurement of glass-like carbons conductivity mechanisms without causing sample damage.

## CRediT authorship contribution statement

**Jaspa Stritt:** Writing – review & editing, Writing – original draft, Visualization, Methodology, Investigation, Formal analysis, Data curation, Conceptualization. **Jerome A. Cuenca:** Writing – review & editing, Supervision, Software, Resources, Methodology, Investigation, Formal analysis, Data curation, Conceptualization. **Evan L.H. Thomas:** Writing – review & editing, Supervision, Methodology, Conceptualization. **Oliver A. Williams:** Writing – review & editing, Supervision,

Resources, Project administration, Methodology, Funding acquisition, Conceptualization.

## Declaration of competing interest

The authors declare the following financial interests/personal relationships which may be considered as potential competing interests: Jaspa Stritt reports financial support was provided by Engineering and Physical Sciences Research Council (EPSRC). If there are other authors, they declare that they have no known competing financial interests or personal relationships that could have appeared to influence the work reported in this paper.

## Acknowledgements

We gratefully acknowledge the Engineering and Physical Sciences Research Council (EPSRC) for funding this project under the "Making a miniature Sun" grant (EPSRC Reference EP/V048295/1).

## References

[1] R.E. Franklin, Crystallite growth in graphitizing and non-graphitizing carbons, Proc. R. Soc. Lond. Ser. A Math. Phys. Sci. 209 (1097) (1951) 196–218, http://dx.doi.org/10.1098/rspa.1951.0197, URL https://royalsocietypublishing.org/doi/10.1098/rspa.1951.0197.

[2] G.M. Jenkins, K. Kawamura, Structure of glassy carbon, Nature 231 (5299) (1971) 175–176, http://dx.doi.org/10.1038/231175a0, URL https://www.nature.com/articles/231175a0.

[3] L. Pesin, E. Baitinger, A new structural model of glass-like carbon, Carbon 40 (3) (2002) 295–306, http://dx.doi.org/10.1016/S0008-6223(01)00130-0, URL https://linkinghub.elsevier.com/retrieve/pii/S0008622301001300.

[4] J. Jang, G. Panusa, G. Boero, J. Brugger, SU-8 cantilever with integrated pyrolyzed glass-like carbon piezoresistor, Microsyst. Nanoeng. 8 (1) (2022) 22, http://dx.doi.org/10.1038/s41378-022-00351-9, URL https://www.nature.com/articles/s41378-022-00351-9.

[5] R. Martinez-Duarte, SU-8 photolithography as a toolbox for carbon MEMS, Micromachines 5 (3) (2014) 766–782, http://dx.doi.org/10.3390/mi5030766, URL http://www.mdpi.com/2072-666X/5/3/766.

[6] A. Singh, J. Jayaram, M. Madou, S. Akbar, Pyrolysis of negative photoresists to fabricate carbon structures for microelectromechanical systems and electrochemical applications, J. Electrochem. Soc. 149 (3) (2002) E78, http://dx.doi.org/10.1149/1.1436085, URL https://iopscience.iop.org/article/10.1149/1.1436085.

[7] E.L.H. Thomas, J. Stritt, S. Mandal, M. Imboden, O.A. Williams, Polycrystalline diamond micro-hotplates, Small (2023) 2303976, http://dx.doi.org/10.1002/smll.202303976, URL https://onlinelibrary.wiley.com/doi/10.1002/smll.202303976.

[8] K. Jurkiewicz, M. Pawlyta, D. Zygadło, D. Chrobak, S. Duber, R. Wrzalik, A. Ratuszna, A. Burian, Evolution of glassy carbon under heat treatment: correlation structure–mechanical properties, J. Mater. Sci. 53 (5) (2018) 3509–3523, http://dx.doi.org/10.1007/s10853-017-1753-7, URL http://link.springer.com/10.1007/s10853-017-1753-7.

[9] F.R.D. Tchoubar, Structural evolution of a glassy carbon as a result of thermal treatment between 1000 and 2700°C, Carbon 15 (2) (1977) 7, http://dx.doi.org/10.1016/0008-6223(77)90018-5.

[10] L.L. Ban, D. Crawford, H. Marsh, Lattice-resolution electron microscopy in structural studies of non-graphitizing carbons from polyvinylidene chloride (PVDC), J. Appl. Crystallogr. 8 (4) (1975) 415–420, http://dx.doi.org/10.1107/S0021889875010904, URL http://scripts.iucr.org/cgi-bin/paper?S0021889875010904.

[11] P.J.F. Harris, Fullerene-related structure of commercial glassy carbons, Phil. Mag. 84 (29) (2004) 3159–3167, http://dx.doi.org/10.1080/14786430410001720363, URL http://www.tandfonline.com/doi/abs/10.1080/14786430410001720363.

[12] H. Lorenz, M. Despont, N. Fahrni, N. LaBianca, P. Renaud, P. Vettiger, SU-8: a low-cost negative resist for MEMS, J. Micromech. Microeng. 7 (3) (1997) 121–124, http://dx.doi.org/10.1088/0960-1317/7/3/010, URL https://iopscience.iop.org/article/10.1088/0960-1317/7/3/010.

[13] T. Tsuzuku, K. Saito, Electric conduction in glassy carbons, Japan. J. Appl. Phys. 5 (8) (1966) 738–739, http://dx.doi.org/10.1143/JJAP.5.738, URL https://iopscience.iop.org/article/10.1143/JJAP.5.738.

[14] D. Hunt, G. Jenkins, T. Takezawa, The effect of tensile stress upon the resistivity of a polymeric carbon, Carbon 14 (2) (1976) 105–109, http://dx.doi.org/10.1016/0008-6223(76)90118-4, URL https://linkinghub.elsevier.com/retrieve/pii/0008622376901184.

[15] M. Eichelbaum, R. Stößer, A. Karpov, C.-K. Dobner, F. Rosowski, A. Trunschke, R. Schlögl, The microwave cavity perturbation technique for contact-free and in situ electrical conductivity measurements in catalysis and materials science, Phys. Chem. Chem. Phys. 14 (3) (2012) 1302–1312, http://dx.doi.org/10.1039/C1CP23462E, URL http://xlink.rsc.org/?DOI=C1CP23462E.

[16] M.B. Isichenko, Percolation, statistical topography, and transport in random media, Rev. Modern Phys. 64 (4) (1992) 961–1043, http://dx.doi.org/10.1103/RevModPhys.64.961, URL https://link.aps.org/doi/10.1103/RevModPhys.64.961.

[17] D. Stauffer, A. Aharony, A. Aharonî, Introduction to Percolation Theory, Rev. second ed., transferred to digital print, Taylor & Francis, London, 2003.

[18] J.C. Dyre, T.B. Schrøder, Universality of ac conduction in disordered solids, Rev. Modern Phys. 72 (3) (2000) 873–892, http://dx.doi.org/10.1103/RevModPhys.72.873, URL https://link.aps.org/doi/10.1103/RevModPhys.72.873.

[19] J.C. Dyre, P. Maass, B. Roling, D.L. Sidebottom, Fundamental questions relating to ion conduction in disordered solids, Rep. Progr. Phys. 72 (4) (2009) 046501, http://dx.doi.org/10.1088/0034-4885/72/4/046501, URL https://iopscience.iop.org/article/10.1088/0034-4885/72/4/046501.

[20] P. Bruce, High and low frequency Jonscher behaviour of an ionically conducting glass, Solid State Ion. 15 (3) (1985) 247–251, http://dx.doi.org/10.1016/0167-2738(85)90010-4, URL https://linkinghub.elsevier.com/retrieve/pii/0167273885900104.

[21] D. Almond, A. West, Mobile ion concentrations in solid electrolytes from an analysis of a.c. conductivity, Solid State Ion. 9–10 (1983) 277–282, http://dx.doi.org/10.1016/0167-2738(83)90247-3, URL https://linkinghub.elsevier.com/retrieve/pii/0167273883902473.

[22] O. Kamishima, Y. Iwai, J. Kawamura, Small power-law dependence of ionic conductivity and diffusional dimensionality in alumina, Solid State Ion. 281 (2015) 89–95, http://dx.doi.org/10.1016/j.ssi.2015.09.011, URL https://linkinghub.elsevier.com/retrieve/pii/S0167273815003513.

[23] J.C. Dyre, Universal low-temperature ac conductivity of macroscopically disordered nonmetals, Phys. Rev. B 48 (17) (1993) 12511–12526, http://dx.doi.org/10.1103/PhysRevB.48.12511, URL https://link.aps.org/doi/10.1103/PhysRevB.48.12511.

[24] D. Halliday, R. Resnick, J. Walker, Principles of Physics, Wiley, 2014, Google-Books-ID, DCqZoAEACAAJ.

[25] D.K. Schroder, Semiconductor material and device characterization, in: Semiconductor Material and Device Characterization, John Wiley & Sons, Inc., Hoboken, NJ, USA, 2005, pp. i–xv, http://dx.doi.org/10.1002/0471749095.fmatter, URL https://onlinelibrary.wiley.com/doi/10.1002/0471749095.fmatter.

[26] J.A. Cuenca, E. Thomas, S. Mandal, O. Williams, A. Porch, Investigating the broadband microwave absorption of nanodiamond impurities, IEEE Trans. Microw. Theory Tech. 63 (12) (2015) 4110–4118, http://dx.doi.org/10.1109/TMTT.2015.2495156, URL http://ieeexplore.ieee.org/document/7330045/.

[27] J.A. Cuenca, E. Thomas, S. Mandal, O. Williams, A. Porch, Microwave determination of sp2 carbon fraction in nanodiamond powders, Carbon 81 (2015) 174–178, http://dx.doi.org/10.1016/j.carbon.2014.09.046, URL https://linkinghub.elsevier.com/retrieve/pii/S0008622314008987.

[28] J.A. Cuenca, S. Mandal, J. Stritt, X. Zheng, J. Pomeroy, M. Kuball, A. Porch, O.A. Williams, Dielectric properties of diamond using an X-band microwave split dielectric resonator, Carbon 221 (2024) 118860, http://dx.doi.org/10.1016/j.carbon.2024.118860, URL https://linkinghub.elsevier.com/retrieve/pii/S0008622324000770.

[29] A.C. Ferrari, J. Robertson, Interpretation of Raman spectra of disordered and amorphous carbon, Phys. Rev. B 61 (20) (2000) 14095–14107, http://dx.doi.org/10.1103/PhysRevB.61.14095, URL https://link.aps.org/doi/10.1103/PhysRevB.61.14095.

[30] A.C. Ferrari, J. Robertson, Resonant Raman spectroscopy of disordered, amorphous, and diamondlike carbon, Phys. Rev. B 64 (7) (2001) 075414, http://dx.doi.org/10.1103/PhysRevB.64.075414, URL https://link.aps.org/doi/10.1103/PhysRevB.64.075414.

[31] R. French, R. Abou-Rahme, D. Jones, L. McNeil, Absorption edge and band gap of $SiO_2$ fused silica glass, Ceram. Trans. 4 (1992) 63–64.

[32] G.-L. Tan, M.F. Lemon, R.H. French, Optical properties and London dispersion forces of amorphous silica determined by vacuum ultraviolet spectroscopy and spectroscopic ellipsometry, J. Am. Ceram. Soc. 86 (11) (2003).

[33] Kayaku Advanced Materials, SU-8 3000 Technical Data Sheet, first ed., Kayaku Advanced Materials, 2020.

[34] R.R. Saxena, R.H. Bragg, Electrical conduction in glassy carbon, J. Non-Cryst. Solids 28 (1) (1978) http://dx.doi.org/10.1016/0022-3093(78)90073-X.

[35] J. Turło, K. Rozwadowska-Jaśniewska, Optical and electrical energy gap investigations in low-temperature glassy carbon layers, J. Non-Cryst. Solids 90 (1–3) (1987) 641–644, http://dx.doi.org/10.1016/S0022-3093(87)80505-7, URL https://linkinghub.elsevier.com/retrieve/pii/S0022309387805057.

[36] N. Xie, W. Shao, L. Zhen, Percolation in disordered conductor/insulator composites, in: Advanced Composite Materials: Properties and Applications, De Gruyter Open, 2017, pp. 440–467, http://dx.doi.org/10.1515/9783110574432-009, URL https://www.degruyter.com/document/doi/10.1515/9783110574432-009/html.

[37] M. Hotta, M. Hayashi, M.T. Lanagan, D.K. Agrawal, K. Nagata, Complex permittivity of graphite, carbon black and coal powders in the ranges of X-band frequencies (8.2 to 12.4 GHz) and between 1 and 10 GHz, ISIJ Int. 51 (11) (2011) 1766–1772, http://dx.doi.org/10.2355/isijinternational.51.1766, URL http://www.jstage.jst.go.jp/article/isijinternational/51/11/51_11_1766/_article.

[38] K. Rubrice, X. Castel, M. Himdi, P. Parneix, Dielectric characteristics and microwave absorption of graphene composite materials, Materials 9 (10) (2016) 825, http://dx.doi.org/10.3390/ma9100825, URL http://www.mdpi.com/1996-1944/9/10/825.